

An assessment of the reproducibility of the Gemini retro focusing system

Contact david.carroll@strath.ac.uk

D.C. Carroll, M. Coury, G. Scott*, P. McKenna

Department of physics, University of Strathclyde, SUPA,
Glasgow G4 0NG, UK

M.J.V. Streeter, H. Nakamura, Z. Najmudin

Physics Department, Imperial College London, London, SW7
2AZ, UK

F. Fiorini, S. Green

School of Physics and Astronomy, University of Birmingham,
Birmingham B15 2TT, UK

**J.S. Green, P. Foster, R. Heathcote, K. Poder, D. Symes,
R.J. Clarke, R. Pattathil, D. Neely**

*Central Laser Facility, STFC RAL, Oxfordshire OX11 0QX,
UK

Introduction

In the Astra-Gemini target chamber solid targets are positioned relative to the tight focus of the laser for an F/2 off-axis parabolic mirror (OAP) using a retro-focusing system. This system uses the focusing OAP itself to collect back-scattered light from the target and sends it back along the beam path. A leak of this light is taken through a mirror and focused down onto a camera. The camera is positioned relative to the focusing lens such that the backscattered light is at tight focus on the camera at the point where the target is at the tight focus position of the OAP.

In this report we present results from a test of the retro-focusing system. The test looked at the repeatability of bringing a target to focus with the system by a single user. We also compared repeatability across multiple users. This is important as positioning the target consistently in relation to the laser focus is essential for solid target experiments.

Astra-Gemini Retro-focus system

The retro focusing system for Astra-Gemini, see figure 1, uses a green (532 nm) laser injected through the back of a high reflectivity dielectric infra-red mirror which is matched to the main laser. The retro system images the green light back scattered from the target. The green laser is used to maximise light collected on camera (using infra-red would result in a much weaker signal through a high reflectivity dielectric infra-red mirror) and the shorter wavelength means a tighter diffraction limited focal spot. This in turn means, if the system is fully optimised, that the green laser will focus and defocus faster than the infra-red laser light and so make it potentially easier for operators to bring targets to focus.

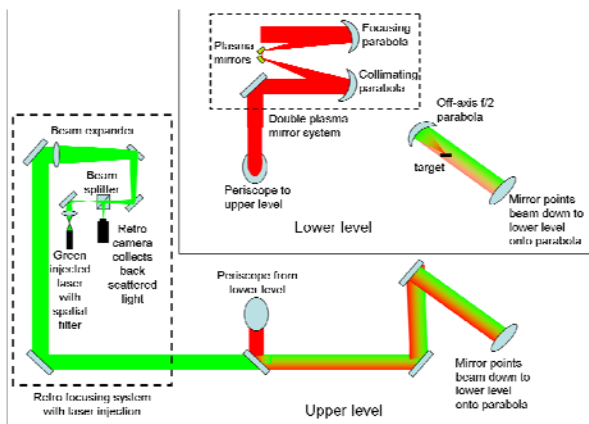


Fig 1: Astra Gemini Beam path with Retro system layout. It also shows how the beam path is split between an upper and a lower level in the chamber.

Retro-focus system test procedure

A solid target with a flat surface, see figure 2, is used for the test, the target is the flat side of a 3 mm diameter Al stalk. The

target is mounted on a three-dimensional motorised stage (dc motors) with magniscales that record the position of the target. The incident angle of the laser, focused with an F/2 OAP, onto target is 35 degrees.

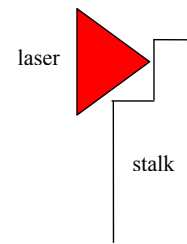


Fig 1: target stalk that was retro focused with.

Five operators of various levels of experience in conducting experiments at the Central Laser Facility were asked to bring the target to the tight focus position of the laser five times in a row. Each operator looked at the retro focus system monitor and attempted to bring it to best focus (minimised spot size as they judged it) by moving the target along its z-axis, which is set by eye to be parallel to the focusing axis of the parabolic mirror. When the operator believed the target to be at tight focus the position value on the magniscale was recorded.

Results

The results of different operators' multiple attempts to bring the target to tight focus are presented in table 1. The operators combined mean position was 1008.5 μm with a standard deviation of 15.5 μm . The full range of values within this is 57 μm (27.5 μm below mean and 29.5 μm above mean). For the purpose of this report the mean position of all operators attempts at bringing the target to tight focus is assumed to be the tight focus position.

The size of the focal spot of the laser in infra-red has previously been measured to be $\sim 2.5 \mu\text{m}$ diameter (d_0 , FWHM) [1]. The focal spot distribution is closer to a super Gaussian than a Gaussian, this means that the radius at $1/e^2$ (otherwise known as the beam waist, w_0) has the following relation to the FWHM: $w_0 = 0.65d_0$. The beam waist is important as it enables us to calculate the Rayleigh range, z_R , of the Astra-Gemini laser with an F/2 parabola:

$$z_R = \frac{\pi w_0^2}{\lambda}$$

Where λ is the laser wavelength, this is 800 nm for the Astra-Gemini laser. The Rayleigh range is 10.4 μm . Note that if the beam spot was a Gaussian distribution then $z_R = 17.7 \mu\text{m}$.

The standard deviation of the mean tight focus position for all operators (15.5 μm) is $\sim 50\%$ greater than the Rayleigh range for a super Gaussian spot (10.4 μm). Only one operator had their

standard deviation just within the Rayleigh range but even then the difference between their lowest and maximum value positions was double the Rayleigh range.

operator	position z (mm)	Mean (mm)	standard deviation	Min (mm)	Max (mm)	Max-Min (mm)
1	1.003	1.0028	0.014618	0.981	1.022	0.041
5 years experience	1.022					
	1.006					
	0.981					
	1.002					
2	1.025	1.018	0.015411	1.001	1.038	0.037
less than 1 year experience	1.004					
	1.038					
	1.001					
	1.022					
3	1.007	1.00800	0.011726	0.99	1.019	0.029
less than 1 year experience	0.99					
	1.019					
	1.018					
	1.006					
4	1.007	0.996	0.008093	0.986	1.007	0.021
5 years experience	0.986					
	0.996					
	1					
	0.991					
5	0.988	1.0178	0.018377	0.988	1.034	0.046
1 year experience	1.013					
	1.029					
	1.025					
	1.034					
Combined values		1.00852	0.015541	0.981	1.038	0.057

Tab. 1: The motor positions for five attempts at getting the target at tight focus for five different operators are listed. The average value for each operator and the overall average are listed along with the standard deviation, the minimum and maximum position values and the difference between these.

When looking at individual operators multiple attempts at focusing there was no trend (limited over 5 attempts) of later attempts getting closer together. If operators got use to retro focusing and became more consistent we would expect later attempts to be closer together.

operator	Mean (mm)	difference between operator mean and overall mean (μm)
1	1.0028	-5.72
2	1.018	9.48
3	1.00800	-0.52
4	0.996	-12.52
5	1.0178	9.28
overall	1.00852	

Tab. 2: The average positions for the five operators and the differences between these values and the overall average.

If we look at individual operators average positions compared to the overall average position for all operators, we find that only one operator (admittedly the most self consistent) was just outside the Rayleigh range when comparing the differences between the individual averages to the overall group average,

see table 2. This is considerably more consistent compared to the standard deviation of the individual attempts.

Conclusions

The retro-focusing system in the Astra-Gemini target area was tested for reproducibility for operators and across multiple operators.

We recommend that with the current retro-focusing system, when bringing the target to best focus an average of multiple positions should be taken. It was found that all operators were either within or very close to the Rayleigh range when comparing individual averages to the overall average position.

This is especially important as the current trend for experiments on Astra-Gemini is the use of multiple shifts to maximise the utilisation of laser time. This means that there is a greater reliance on consistency of target alignment across multiple operators.

Relying on getting close to best focus with a single attempt, even after multiple attempts, is not recommended as only one operator was consistent enough to have a standard deviation within the Rayleigh range and one other operator with a standard deviation close to the Rayleigh range. Even for these operators the differences between minimum and maximum positions was much greater than the Rayleigh range.

There are several ongoing projects to improve the positioning of the target relative to focus currently being investigated for Gemini. These include adding a wavefront sensor to the current retro-focusing system which will enable the focusing parameter of the wavefront to be used to aid target positioning. Another project is the development of a modified interferometric target positioning system as an alternative to the retro-focusing system, this has the potential for sub-micron accuracy.

References

1. D.C. Carroll *et al*, New Journal of Physics **12** 045020 (2010)

Modelling of relative delay for scattered rays in a grating stretcher

Contact Oleg.Chekhlov@stfc.ac.uk

O.Chekhlov, C J Hooker,

Central Laser Facility, STFC Rutherford Appleton Laboratory, Chilton, Didcot, Oxon, OX11 0QX

Introduction

One of the issues of compressed pulse contrast in the chirped pulse amplification (CPA) technique is the picosecond pedestal around the main peak of the pulse. Despite the common understanding [1,2] that some noise in spectral amplitude or spectral phase is responsible for the pedestal, the source of this modulation is still not clear. Suspected sources of noise include scattered light from the surfaces of the optical elements and mainly on the diffraction gratings of stretchers and compressors. We have shown in our experimental studies [3] that the gratings in our pulse stretcher are the main source of the pedestal. The scattering on the surfaces of diffraction gratings has been studied in different spectral regions both theoretically and experimentally [3,4]. However, the effect of scattering on pulse compression quality must be tested from several points of view. In this article we analyse a scenario for scattered light to contribute to the pedestal of the compressed pulse by adding noise in the group delay dependence of the stretcher. We assume that light at a particular wavelength scattered at both the first and the second diffraction gratings could find shorter and longer paths through the pulse stretcher. The scenario is based on an assumption that light scattered in different directions can return to the starting point of the stretcher and scatter into the direction of the output pulse within the acceptance angle of the system. Estimates of possible delays for scattered beams inside the Astra stretcher have been obtained from a Zemax model of a grating pulse stretcher with parameters similar to the one used in Astra.

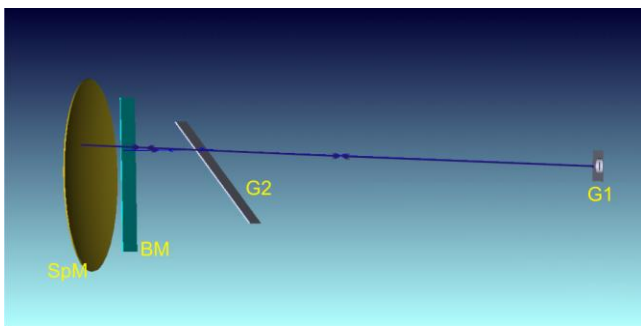


Figure 1. Schematic of the Astra pulse stretcher, which consists of a small diffraction grating G1, large grating G2, back mirror (BM) and spherical mirror (SpM).

Modelling scattered light in the Astra pulse stretcher

As a working idea we assume that a scattered beam might be advanced or delayed if the scattered light travelled along different paths in the stretcher, in directions that are not governed by the laws of diffraction, and then returns to its starting point in the stretcher. If we first consider a path with two scattering events, on the first grating (G1) and the second grating (G2), then we can easily predict that a median route for the beam would be the one which had a reflection on the back mirror (BM) and a return point on G1 that coincided with the starting point. On the assumption that scattering is happening at every reflection from a diffraction grating, we need to estimate the delay for every path along the route G1-SpM-G2-BM-G2-SpM-G1 that involves reflection at SpM and BM, but in which

the rays can depart from each grating at a range of angles due to the scattering.

To simulate the scattering process in Zemax, the model was set up so that at each point where the ray under investigation was incident upon a grating, the model could use either a diffraction grating at the correct orientation, or a mirror with variable rotation angle. Changing the angle of the mirror at the point of incidence gave the effect of a fan of rays spread out in the dispersion direction, simulating the propagation of scattered light. The distance the light travelled through the stretcher could be calculated for a range of angles. To discriminate between the beams returning to G1 we used the criterion that a returning scattered beam might contribute to the pedestal of the compressed pulse if it was incident on G1 within 1 mm of the centre of the input beam.

The parameters of the Astra stretcher are such that an optical pulse with a spectrum of 30nm FWHM would be stretched to 566 ps. The data presented below were obtained for this stretch factor, which corresponds to 1050 mm separation between G1 and G2, SpM at 1400mm from G1 and BM 350mm from G2.

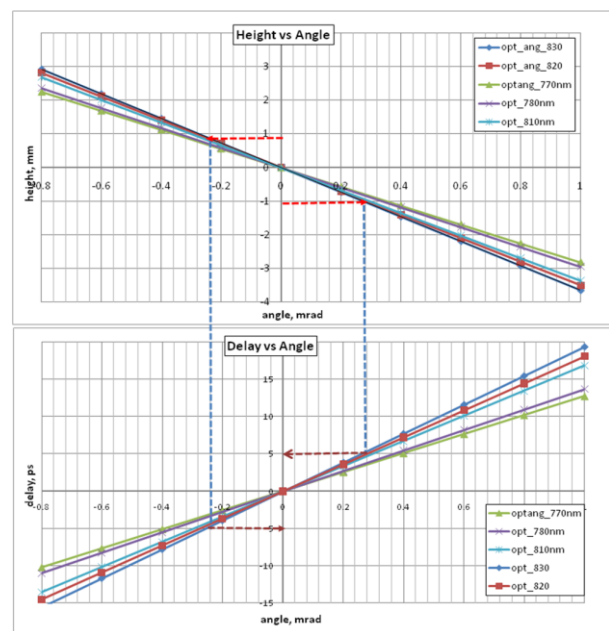


Figure 2. Dependences of the relative height of the returning beams at G1 on the relative angle of the input G1 mirror (upper plot), and corresponding relative delays of the output beams as a function of scattering angle.

The average stretch factor for the 36.3 degree grating angle is 18.9 ps/nm. The angular spread of a spectrum with 30nm spectral width is 3.15 degrees. An average linear stretch factor in angles would be ~ 179.7 ps/degree. The data in Figure 2 are presented as the relative position ('height') of the returning beam scattered beam at G1 as a function of angle of rotation of the G1 mirror relative to a median direction of the input monochromatic beam (top plot in Fig.2). Corresponding delays at these angles are plotted in the lower part of Fig.2. Several

parameters could be retrieved from this set of data as a function of varying stretcher settings. As can be seen from the upper plot in Figure 2, the returning rays fall within a height range of ± 1 mm at G1 only for angles in a range of ± 0.31 mrad. The maximum delay for this angle range is estimated as 9.77 ps. It should be pointed out that the data in Fig.2 are very similar to each other even though they were obtained for different wavelengths. The similarity is caused by the stretcher geometry and angle of the diffraction gratings. The lines on the delay plot represent variation of the optical path L through the stretcher with input angle $(dL/d\theta)/c|_{\theta}$ for each chosen wavelength, where c - speed of light. The variation of the delay as a function of relative rotation of G1 mirror at 800nm was estimated as ~ 15.7 ps /mrad.

Similar measurements of optical path delay and relative height at G1 have been made as a function of the rotation of G2 treated as a mirror. After reflecting from the mirror the rays propagated to BM and back to G2 grating, and after a normal diffraction event at G2 the rays were returned to G1 by the spherical mirror. The ray heights and their delays at G1 varied linearly with the relative rotation angle of G2 mirror, with a slope of ~ 7.54 ps/mrad at 800nm. Although the slope of the G2 mirror delay dependence appeared to be smaller than that of G1 mirror the range of G2 mirror angles satisfying the condition of ± 1 mm relative height at G1 was larger: ± 0.72 mrad at 800 nm. Consequently the maximum delay between the rays appeared to be larger (~ 10.9 ps) than that coming from G1. The difference in angle range seems to be due to the greater distance of the G1 mirror from the output spot. The dependences of total delays over the 2mm height change (± 1 mm relative height) for G1 mirror and G2 mirror scans are plotted in Figure 3.

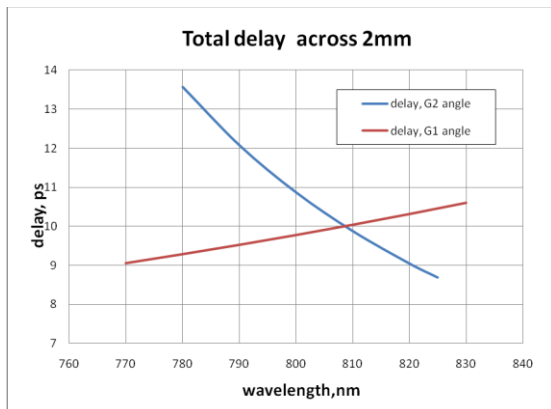


Figure 3. Wavelength dependences of total delay across ± 1 mm relative height at G1 position: red = angle source at G1; blue -angle source at G2 position.

To measure a combined delay of rays experiencing double scattering events, the Zemax model used both simulated sources of scattered angles on G1 and on G2 gratings. The results of the delay measurements carried out at 800 nm wavelength are presented in Figure 4 as dependence on two rotation angles of G1 mirror and G2 mirror. The two-parametric dependence in Figure 4 is a flat surface built from two linear dependencies with different slopes in two perpendicular directions. We are interested in estimating the maximum possible delay between two rays of the same colour that satisfy the criterion of ± 1 mm relative height. The flat tilted plane of the delay dependence is colored according to the relative height of the rays at the output plane. The delays for the rays with ± 1 mm height at the output plane lie within the range of G1/G2 angles which are indicated by a yellow – blue band on the delay dependence. The extreme delay conditions between the scattered rays are indicated by the arrow's ends in Fig.4. The maximum delay for the rays at 800nm and range angles of rotation is estimated at 26ps. The combinations of angles for G1/G2 mirror rotations that correspond to the maximum delays was estimated as $\sim (\pm)0.58$ mrad/ $(\pm)1$ mrad (of the same sign). These angles are

larger than those estimated for the single angle rotation, because of the fact that G1 and G2 mirror angles are in the same plane means they can partially compensate each other. The maximum delay between extreme rays which satisfied our chosen criterion of ± 1 mm of the relative height at the output plane was close to the value of the pedestal width usually observed in pulse contrast measurements. The maximum delays for other wavelengths are expected to be similar to the delay of 800nm beam.

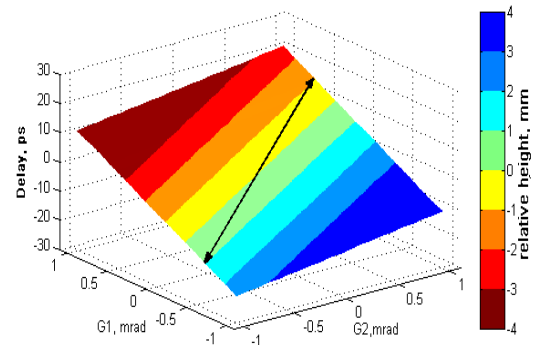


Figure 4. Dependence of relative delay of ray propagation through the stretcher on angle rotation of G1 and G2 mirrors. The colour map corresponds to the relative height of the rays at G1 position.

The map of delays presented in Fig.4 could be helpful in estimating delays using the measured scattering function of a diffraction grating. The range of delays for a smaller relative height could also be estimated from the map, and this would be smaller as well. We should make it clear that the estimates of relative delay presented here do not confirm that the appearance of a coherent pedestal on the contrast traces is due to scatter, but are intended to model a plausible scenario incorporating noise from scattered light through group delay spectral dependence. The delay estimated here for scattered rays in the stretcher is mainly caused by the geometry of the diffraction grating tilt, so the delays are expected to be different for designs with different central wavelength or diffraction angle.

References

1. K.-H. Hong, B. Hou, J. A. Nees, E. Power, and G. A. Mourou, *Appl. Phys. B* **81**, 447–457(2005)
2. C.Dorrer, J.Bromage, *Optics Express* **15**, 3058-3068(2008).
3. C.J.Hooker, Y. Tang, O. Chekhlov, J. Collier, E. J. Divall, K. Ertel, S. J. Hawkes, B. T. Parry and P.P Rajeev, *Optics Express* **19** No. 3, 2193-2203, 31 January 2011
4. E. Marx, T. A. Germer, T. V. Vorburger, B. C. Park, *Applied Optics* **39**, 4473-448 (2000).

Characterization and correction of the Gemini wavefront

S Hawkes, C J Hooker, B Parry

Central Laser Facility, CLRC Rutherford Appleton Laboratory, Chilton, Didcot, Oxon. OX11 0QX

Main contact email address: steve.hawkes@stfc.ac.uk

Introduction

The wavefront quality of any ultra short laser system is of fundamental importance as it determines the on target intensity. The wavefront quality of the Gemini beams has been characterized and a static correction of the aberrations implemented. Measurements were made at the output of the Gemini amplifier and after the pulse compressor using a HASO 32 Shack-Hartman wavefront sensor. Additional measurements were made using a SID 4 shearing interferometer wavefront sensor.

CW beam measurements

A CW alignment beam is used to align the Gemini amplifier and is locally generated in the Gemini laser area. This comprises an 810nm diode focused through a diffraction limited pinhole and collimated at 50mm diameter. This beam is injected immediately before the beamsplitter which separates the North and South beams. The Astra beam is injected perpendicular to the CW beam allowing both beams to present at the same time, a sliding beam block can be moved in to block the CW beam if required. Measurements made of this beam indicate that this is good quality and produces a close to diffraction limited performance. The CW beam has an overall Peak to Valley (PV) distortion of 0.3 waves. As this beam is used to optimize the final focusing optics in the Gemini Target Area it is of critical importance that it be as good as possible. The measured wavefront and first 30 Zernike coefficients are presented in figure 1

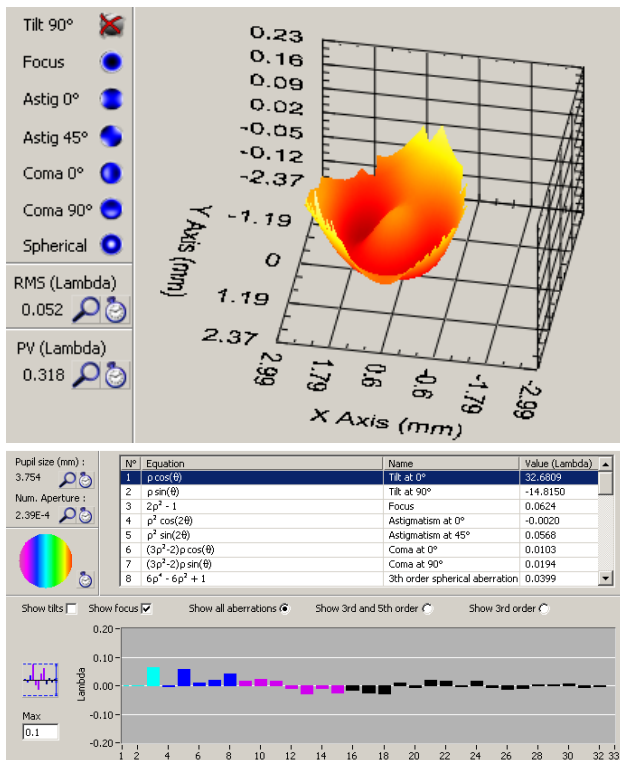


Figure 1. CW Wavefront distortion and Zernike coefficients

Initial Characterization

The Gemini amplifiers are of a 4 pass geometry and present a significant extension to the optical path of the Astra laser

system. Measurements were made of the wavefront quality of the Astra 10 Hz beam at the output of the Gemini south amplifier. The overall PV distortion of the beam was found to be 0.9 waves with the most significant contribution coming from an astigmatism measuring 0.5 waves, this represented by the 4th Zernike coefficient and is presented in figure 2. This is produced by a combination of aberrations generated in the Astra laser and further contributions from the additional optics in the Gemini amplifier.

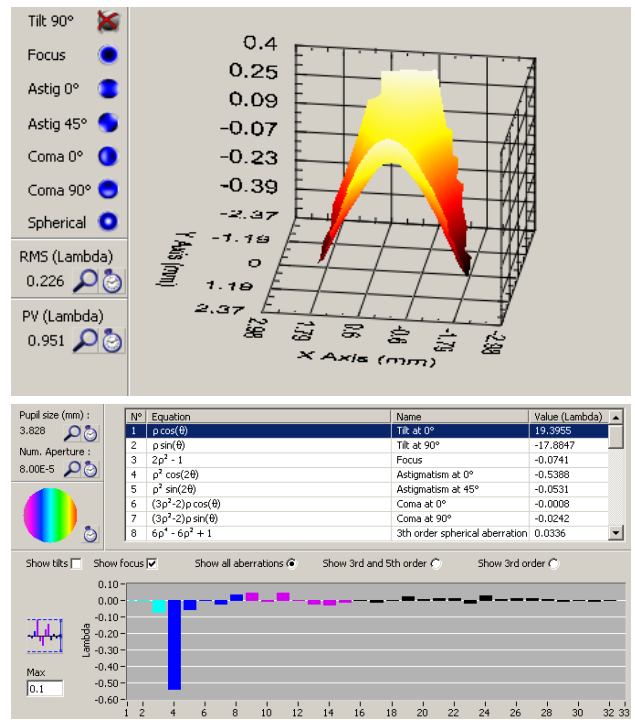


Figure 2. Astra 10 Hz Wavefront distortion and Zernike coefficients

Variation with Astra energy

The amount of astigmatism, measured at the output of the Gemini amplifier, is seen to vary (see figure 3) depending on the output energy of the Astra laser. In turn, this variation of energy of the Astra laser is caused by a change in the pump energy loading on the Ti:Sapphire crystal and the amount of extracted energy which affects the thermal lens of the crystal.

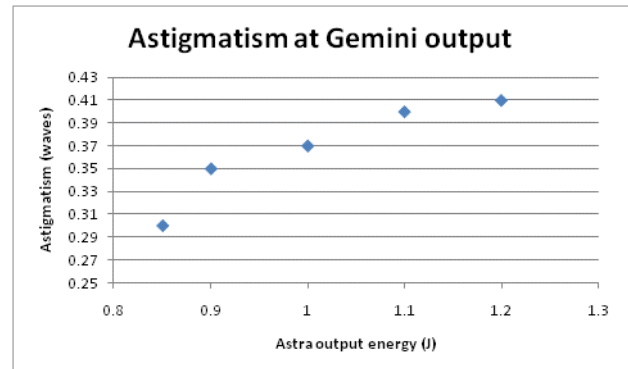


Figure 3. Astigmatism with Astra energy

Implementation of a static corrector

In order to correct the aberrations on the Gemini beam, generated from both the Astra 10 Hz beam and those static aberrations in the Gemini amplifier a Static Aberration Corrector (SAC) was deployed. The SAC generates astigmatism by physically bending a standard zero degree incidence infrared mirror using force applied by micrometers (see figure 4). The SAC comprises of a central ring into which the mirror sits, two rings, of smaller inner radius, then bolt onto the central ring, effectively clamping the mirror inside the central ring. The four micrometers are then driven through the outer two rings so as to make contact with the mirror, force is then applied to the mirror, as in figure 4, so as to produce an astigmatism. An equal and opposite amount of astigmatism, at the required orientation is generated to correct the astigmatism on the beam. The SAC was installed at the input to the Gemini amplifier as seen in figure 4.

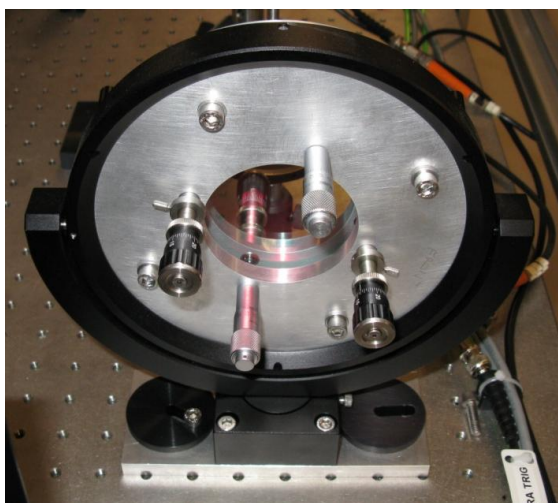
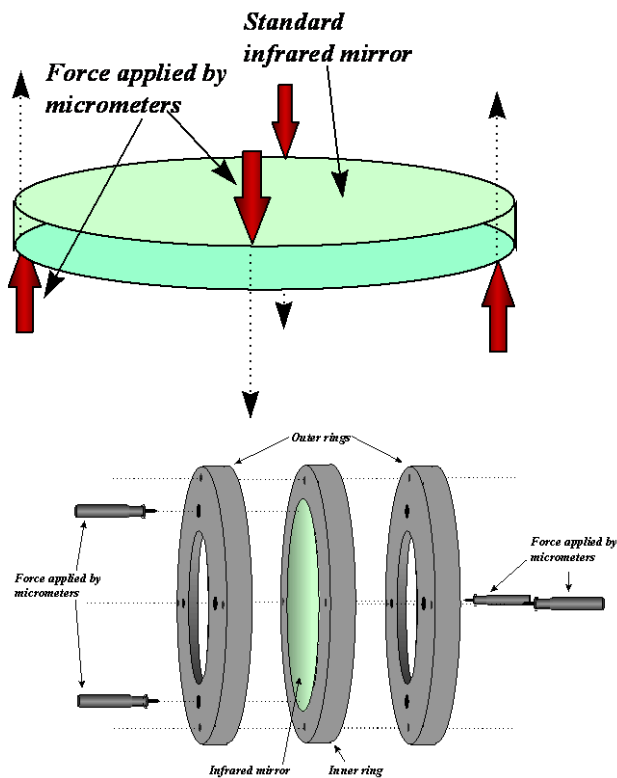


Figure 4. SAC design and implementation

Careful optimization of the SAC in situ significantly reduced the astigmatism on the Gemini beam from 0.5 waves peak to valley to less than 0.1 waves PV. The overall PV wavefront distortion is now at 0.34 waves. (See figure 5). This correction more closely matches the wavefront of the Gemini pulsed beam to that of the locally generated CW beam. Operating experience of the using the SAC with the Gemini beam indicates that occasional adjustment of the SAC is required. As mentioned earlier this is largely due to changes in the thermal lens of the third Astra amplifier. Adjustments are normally made at the start of an experiment to flatten the wavefront as best possible with fine adjustment occasionally made when required.

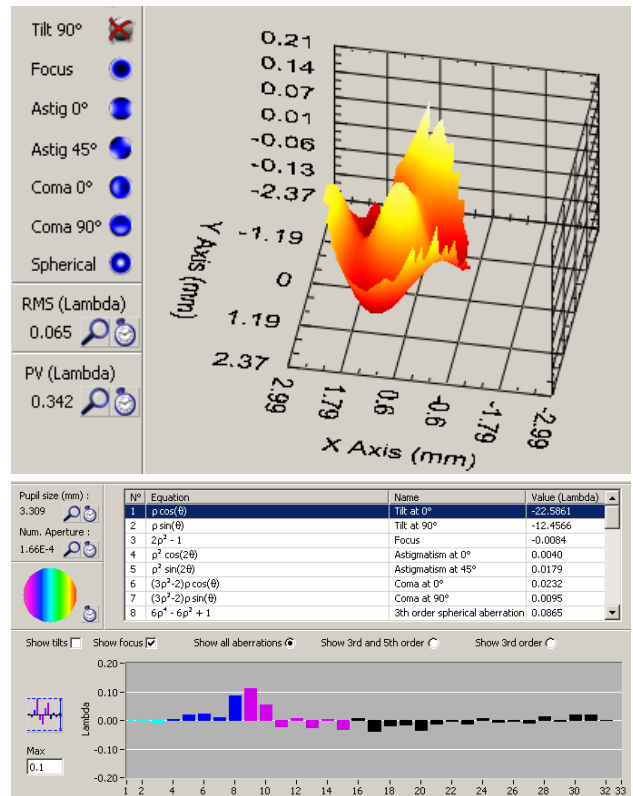


Figure 5. Corrected Astra 10 Hz Wavefront distortion and Zernike coefficients

Conclusions

The wavefront quality of the Gemini CW and repetitively pulsed beams has been characterized using a HASO wavefront sensor. The wavefront has been corrected to 0.3 waves PV using a Static Astigmatism Corrector. Further improvement is still required for the more demanding Gemini experiments and this will require an adaptive optic, which is under development.

Improving the contrast of Astra Gemini

Contact chris.hooker@stfc.ac.uk

C J Hooker, Y Tang, O Chekhlov, J L Collier, E J Divall, K Ertel, S J Hawkes, R P Pattathil and D R Symes

Central Laser Facility, STFC Rutherford Appleton Laboratory, HSIC, Didcot, Oxon OX11 0QX

Introduction

In ultra-intense laser systems used for plasma physics research, contrast is one of the most important properties of the laser pulse. If the pulse has low contrast, a plasma can be formed on the target before the ultrashort compressed pulse arrives, which significantly changes the nature of the interaction [1]. In these circumstances certain types of target, such as ultrathin foils used for ion acceleration, can be completely destroyed prior to the arrival of the main pulse. As future lasers increase in power to tens of PW [2] or exawatts [3], corresponding improvements in pulse contrast will be essential.

The majority of ultra-intense lasers are based on the technique of chirped-pulse amplification (CPA) [4]. In CPA lasers, poor contrast can take the form of amplified spontaneous emission extending over nanoseconds, and discrete prepulses that usually occur within a few hundred picoseconds of the main pulse. A third contribution is uncompressible energy within the stretched pulse, which manifests itself as an exponentially-rising pedestal, typically within 20 picoseconds of the main pulse. This latter feature is termed the “coherent” contrast pedestal, and is of concern because its effect is to extend the leading edge of the pulse by several picoseconds at an intensity which is likely to be well above the plasma generation threshold, leading to the damaging effects noted above. Various pulse cleaning techniques such as double CPA [5], XPW [6] and the use of plasma mirrors [7] can significantly improve the contrast on timescales from nanoseconds down to picoseconds, but become ineffective closer to the main pulse. For this reason it is important to understand the origins of the coherent pedestal (CP) and to find ways of reducing it.

In this article we report a study of the cause of the CP that we carried out using Astra Gemini. The design of the Astra pulse stretcher allowed us to separate the effects of different optical components, and show that the majority of the CP originates from the stretcher gratings.

Contrast measurements

For the majority of this work we used the 10 Hz beam from Astra, a sample of which is available in the short-pulse diagnostic beam emerging from the Gemini pulse compressors. This beam has about ten mJ of energy per pulse, and is used to measure properties of the compressed pulse, including contrast. The contrast diagnostic was a “Sequoia” a commercially-available third-order scanning cross-correlator. The pulse to be measured is split into two parts, one of which is frequency doubled to give a relatively clean pulse thanks to the non-linear nature of the harmonic generation process. The other part of the pulse, at the fundamental wavelength, is scanned through the harmonic pulse by means of a variable time delay, and the third harmonic signal from the mixing of the two pulses is measured for each delay step. The result is a record of the intensity of the main pulse as a function of delay, with a dynamic range that can be ten or eleven orders of magnitude, limited by the dark current of the photomultiplier in the instrument. Figure 1 shows a typical Sequoia scan from Astra, exhibiting the three contrast features referred to above: the ASE baseline at an intensity of

around 10^{-9} , various discrete pre- and post-pulses and a triangular feature occupying the 15 picoseconds either side of the main pulse. The latter feature is the coherent pedestal which is the subject of this article. Similar scans have been published for other CPA laser systems, and they show very similar features. We have made significant progress in determining the origin of this feature and in reducing it.

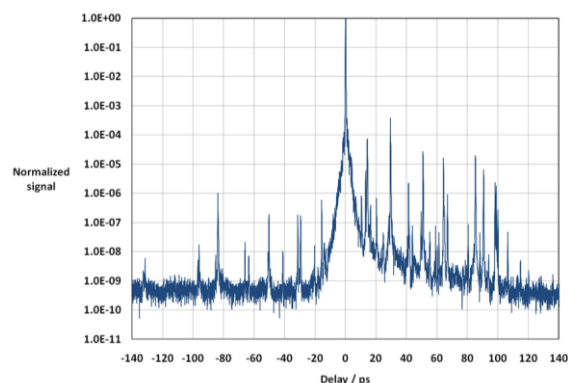


Figure 1. Example contrast scan of the Astra 10 Hz beam.

Experimental study of the coherent pedestal

Determining the origin of the coherent pedestal is difficult in a CPA laser because contrast measurements can be made only on a compressed pulse. Pulses in the rejected kHz train from the front end of Astra have been stretched to a few picoseconds by material dispersion, and can be recompressed using a prism compressor. A contrast scan of these pulses shows no evidence of the CP, so the source must lie further down the laser chain. This agrees with evidence from other systems where the pulse is not stretched [6]. Once the pulse has been stretched it must be recompressed before the contrast can be measured, and this requires a full-sized grating compressor, which in Astra restricts the locations where the measurement can be made to the Astra experimental area and the output of the Gemini compressor. Contrast measurements in either place show a fully-developed pedestal on the pulse [Figure 2], which appears almost identical

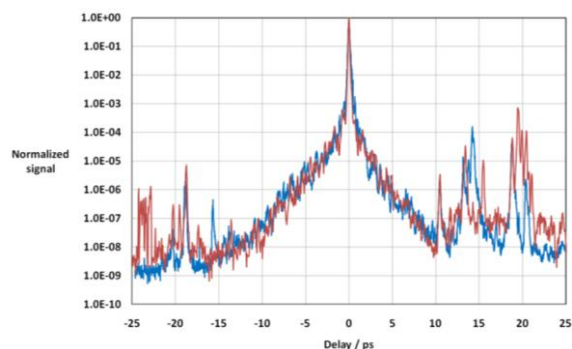


Figure 2. Comparison between single stretched (red) and double stretched (blue) pulses: the coherent pedestals are almost identical.

regardless of whether the pulse has been stretched to only 530 ps by a single pass, or to 1.06 ns by a double pass through the

stretcher optics. The traces shown were obtained several months apart and with two different pulse compressors. It is highly unlikely that two different compressors having different geometries and compensating two different stretches would introduce pedestals that are so similar. This shows that the compressor gratings do not contribute significantly to the CP.

Since the first observation of the CP in Astra in 2006, the laser has undergone many changes, including a complete change of oscillator and preamplifier, a redesign and rebuild of the first amplifier and the introduction of single- and double-pass operation of the pulse stretcher. The CP has remained present throughout and has not been affected by any of these changes. This is a clue that the feature's origin is one of the parts of the laser that has not been changed, which restricts it to the pulse stretcher, the second amplifier and some of the intervening optics. Theoretical studies [8, 9, 10] have shown that noise in the spectrum caused by surface roughness of optical components where the beam is spatially dispersed can lead to the appearance of features with this form. This led us to suspect that the CP originated in the stretcher.

Pulse stretcher configuration and modifications

A schematic layout of the pulse stretcher is shown in Figure 3: part (a) shows a plan view, and part (b) a side view. The path followed by the beam is normally G1-SM-G2-BM-G2-SM-G1, which is indicated in Figure 3(a) & (b) by the red line. This stretcher is not the usual Öffner design, but was developed independently at the CLF [11]. However, other laser systems that do use Öffner-type stretchers, including Vulcan, have similar contrast features in their compressed pulses, so it seems that the design of stretcher does not greatly affect the appearance of the CP.

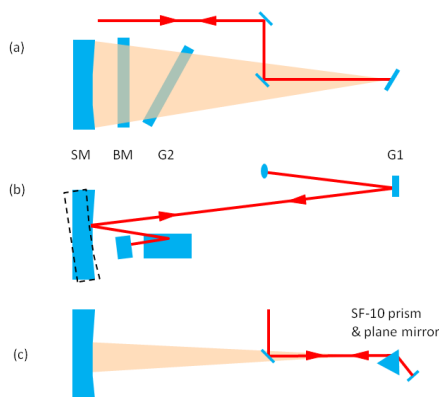


Figure 3. Schematics of the Astra pulse stretcher. Named components are G1: first grating; SM: spherical mirror; G2: second grating; BM: back mirror.

We carried out an extensive set of tests in which components of the stretcher were changed or bypassed entirely, with the aim of determining which of them gave rise to the CP. The first optic replaced was the plane back mirror, BM, which had acquired a significant amount of dust and other contamination. Cleaning the surface using strippable polymer made a clear difference to the visual appearance but did not affect the CP in any way. It was replaced by a new mirror with a broadband dielectric coating, but this also failed to make any difference to the CP. Replacement of the gold-coated input mirror with a new dielectric-coated optic also made no difference.

The design of the Astra pulse stretcher allows some of the components to be bypassed with suitable realignment. The point of incidence of the beam on the first grating is very close to the centre of curvature of the spherical mirror, so by tilting the mirror up as shown by the dashed outline in Figure 3(b) the dispersed light from the grating can be retro-reflected back to

the same point on the grating. The second reflection from G1 reverses the dispersion and recombines the spectral components into a small beam without introducing any time delay between them, which allows the pulse to be compressed in a prism compressor. With this arrangement the beam is not reflected from the second grating or the back mirror, so neither of them has any effect on the contrast.

The result of this test is shown as the red trace in Figure 4. The size of the CP was reduced significantly, so that the point where it intersected the rising edge of the main pulse was a factor of 100 lower than on the reference scan. This demonstrates that a significant part of the CP is due to the second grating, given that cleaning and then replacing the back mirror had no measurable effect. The residual CP, shown by the red trace in Figure 4,

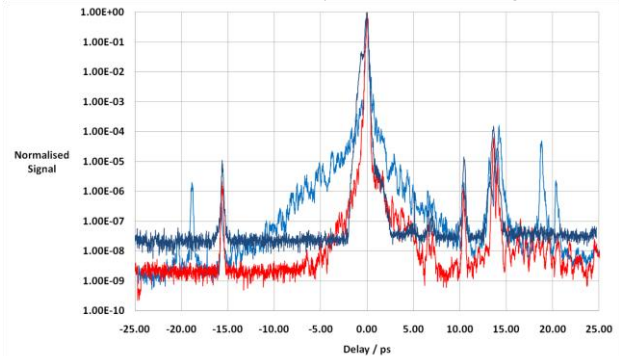


Figure 4. Contrast traces recorded with different configurations of the stretcher optics: Light blue: original trace; red: trace with G2 and BM bypassed; Dark blue: trace with prism in place of G1.

could be due to either the first grating or the spherical mirror. To investigate further, we set up a double-passed prism of SF-10 glass and a plane mirror to replace the first grating, in the arrangement shown in Figure 3(c). The aim was to eliminate the first grating while still dispersing the light on the surface of the spherical mirror.

A contrast scan with the prism arrangement is presented as the dark blue trace in Figure 4. The main pulse is longer than before, because the dispersion from the approximately 4 cm of path in the SF-10 prism could not be fully compensated in the prism compressor. As the signal is normalized to the height of the peak, the baseline of the trace is higher. However, substituting the prism for the grating has reduced the CP by at least another order of magnitude, otherwise it would be visible at the leading edge of the main pulse between -4 and -2 picoseconds. This shows that the residual CP seen when the second grating was bypassed did indeed originate from the first grating, and not from the spherical mirror, which was still present.

Discussion

These results clearly demonstrate that the dominant contribution to the CP comes from the gratings in the pulse stretcher. Previous theoretical work [8, 9, 10] has shown that spectral phase noise in dispersed beams in stretchers can form exponential pedestals like these. Spectral phase noise can arise from surface roughness of components where the beam is spatially dispersed, and this could account for the observed effect of the second grating. However, there is clearly a contribution to the CP from the first grating where the beam is not dispersed. We also observed that cleaning the back mirror, where the beam is dispersed, reduced the scatter but did not affect the CP. This leads to the conclusion that scattering from gratings, irrespective of the beam dispersion on them, is the primary cause of the CP. It may be that the processes involved in manufacturing diffraction gratings generate roughness on a range of spatial scales, whereas the optically polished and coated surfaces of mirrors and prisms are smoother. The origin

of the CP is, however, closely linked with dispersion. When gratings disperse light, wavelength components scattered from the gratings could follow a slightly shorter path through the stretcher optics. Such scattered light could leave either grating at a range of angles which would be different from the diffraction angle (for any given wavelength), and could, in principle, travel along a shorter path through the stretcher back to the first grating. This possibility has been studied theoretically using the optical modelling code Zemax, and some results are presented elsewhere in this report. The acceptance angle into the subsequent optics would restrict the range of delays that could propagate further down the laser chain. This could account for our observation that the size and shape of the CP remain unchanged regardless of whether the pulse is singly or doubly stretched. We note that the CP has an exponential form, appearing linear in the logarithmic plots, and that typical scatter distribution functions also show an exponential variation with angle [12].

Scatter measurements on the gratings

The results described above highlighted the need to replace the gratings in the stretcher. While doing this, we made some simple scatter measurements: on the new gratings before installation and on the old gratings after they were removed from the stretcher. The grating was mounted with its dispersion direction horizontal, and a fibre-coupled 800 nm CW diode laser with a collimated 3 mm diameter beam was incident on it at the Littrow angle of approximately 36 degrees. The beam was horizontally polarized to match the condition in the stretcher. An infra-red sensitive CCD camera was used to image the laser spot on the grating in scattered light. The angle of view of the camera relative to the beam was kept constant at 1.9 degrees for each grating tested. In the stretcher itself the relevant scattering angles would be of the order of milliradians, but scatter measurements at such a small angle are very difficult to perform. In this case our aim was simply to compare the amount of scattering from new and old gratings under the same conditions, rather than measure their scatter distribution functions accurately.

To measure the scatter, the peak brightness signal in the image of the spot was recorded for a range of different lens apertures and exposures. The exposure time and lens aperture were adjusted while viewing a line-out through a live image of the scatter spot to ensure the image was not saturated. By comparing the signals obtained at the same exposure and aperture from the new and old gratings, the relative scatter level could be determined. The camera gain and other parameters were kept constant throughout. The data for the old and new second gratings are shown in Table 1.

		New Grating 2	Old Grating 2	
Exposure/ms	Aperture	Peak brightness	Peak brightness	Brightness Ratio
10	F/4	151	900	6.0
10	F/5.6	75	520	6.9
10	F/8	46	310	6.7
5	F/2.8	150	930	6.2
5	F/4	74	480	6.5
5	F/5.6	38	260	6.8

Table 1. Scatter brightness measurements on old & new gratings.

There is clearly a significant difference between the two gratings, with the old grating scattering on average 6.5 times more strongly than the new. A similar measurement on the two first gratings showed a smaller factor of 2.5, with the old grating again having the larger scatter.

Replacement of stretcher gratings

The original gratings are gold-coated holographic photoresist gratings with a sinusoidal groove shape. The two new gratings were obtained from Plymouth Grating Laboratories, and are etched binary gratings, which have an approximately rectangular groove shape. The grating structure is first formed in photoresist, then etched into the silica substrate before being gold coated. This process improves the damage resistance, and the rectangular groove form also gives significantly higher diffraction efficiency in the 750-850nm spectral region: the average efficiency measured at 805 nm is 94% in first order for the new second grating, and 91.5% for the first. The new second grating has an excellent figure, with a peak-to-valley error of 0.09 wave and an RMS error of 0.013 wave. The old grating has a peak-to-valley error of 0.25 wave and an RMS error of 0.035, which is significantly worse, although the P-V error appears mainly as an overall smooth curvature of the surface.

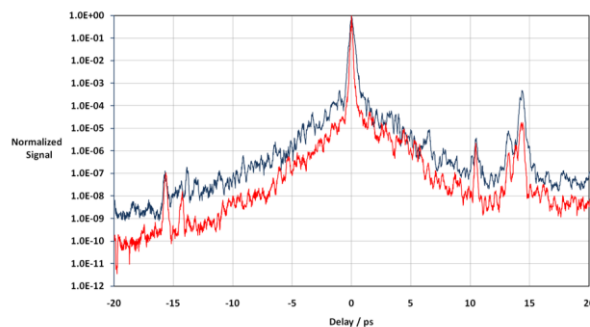


Figure 5. Contrast scans recorded before (blue) and after (red) the change to new gratings in the pulse stretcher.

After installing the new gratings and optimizing the pulse duration, a contrast scan was made, which is shown in Figure 5. With the new gratings the level of the CP was reduced by more than an order of magnitude. More accurately, taking the ratio of the signal levels at each delay and averaging them gives a factor of 21 for the reduction in amplitude of the CP. This factor is similar to the product of the relative scattering factors of the gratings measured above, which supports our conclusion that scattering from gratings is the principal cause of the CP.

Conclusions

We have investigated the origin of the coherent contrast pedestal of the Astra Gemini titanium-sapphire laser system. By making contrast measurements with several optical configurations of the pulse stretcher, in which different components were eliminated or replaced, we were able to distinguish the contribution to the CP from different optics. Our results show that scatter from the diffraction gratings in the pulse stretcher is the main source of the CP. Scatter from mirrors, and dispersion by a prism with polished surfaces, did not make a measurable contribution to the CP. The essential factor in generating a CP therefore appears to be scatter from the diffraction gratings. Installing new higher quality gratings in the Astra pulse stretcher has resulted in an order-of-magnitude reduction in the intensity of the CP, a significant improvement in the overall contrast of the compressed pulse from the laser. The etching process used for the new gratings may yield a smoother surface, giving lower scatter and leading to the observed improvement in contrast. In the ten or more years since the original gratings were made, the technology of grating production has advanced in response to the requirements for high-energy CPA lasers, and gratings made today undoubtedly have better quality. Our results suggest, however, that further improvements may be essential, as the coherent pedestal could be the ultimate limit on the contrast available from ultra-intense laser systems.

References

1. D. Neely, P. Foster, A. Robinson, F. Lindau, O. Lundh, A. Persson, C-G.Wahlström, and P. McKenna, "Enhanced proton beams from ultrathin targets driven by high contrast laser pulses," *Appl. Phys. Lett.* **89**, 021502 (2006).
2. C. Hernandez-Gomez, S. P. Blake, O. Chekhlov, R. J. Clarke, A. M. Dunne, M. Galimberti, S. Hancock, R. Heathcote, P. Holligan, A. Lyachev, P. Matousek, I. O. Musgrave, D. Neely, P. A. Norreys, I. Ross, Y. Tang, T. B. Winstone, B. E. Wyborn, and J. L. Collier, "The Vulcan 10 PW Project," *J. Phys.* **244** 032006 (2010).
3. <http://www.extreme-light-infrastructure.eu>.
4. D. Strickland and G. Mourou, "Compression of amplified chirped optical pulses," *Opt. Commun.* **56**, 219–221 (1985).
5. M. P. Kalashnikov, E. Risse, H. Schönnagel, and W. Sandner, "Double chirped-pulse-amplification laser: a way to clean pulses temporally," *Opt. Lett.* **30**, 923–925 (2005).
6. A. Jullien, O. Albert, F. Burgy, G. Hamoniaux, J.-P. Rousseau, J.-P. Chambaret, F. Augé-Rochereau, G. Cheriaux, J. Etchepare, N. Minkovski, and S. M. Saltiel, "10–10 temporal contrast for femtosecond ultraintense lasers by cross-polarized wave generation," *Opt. Lett.* **30**, 920–922 (2005).
7. A. Lévy, T. Ceccotti, P. D'Oliveira, F. Réau, M. Perdrix, F. Quéré, P. Monot, M. Bougeard, H. Lagadec, P. Martin, J.-P. Geindre, and P. Audebert, "Double plasma mirror for ultrahigh temporal contrast ultraintense laser pulses," *Opt. Lett.* **32**, 310–312 (2007).
8. D. N. Schimpf, E. Seise, J. Limpert, and A. Tünnermann, "Decrease of pulse-contrast in nonlinear chirped-pulse amplification systems due to high-frequency spectral phase ripples," *Opt. Express* **16**, 8876–8886 (2008).
9. V. Bagnoud and F. Salin, "Influence of optical quality on chirped-pulse amplification: characterization of a 150-nm-bandwidth stretcher," *J. Opt. Soc. Am. B* **16**, 188–193(1999).
10. C. Dorrer and J. Bromage, "Impact of high-frequency spectral phase modulation on the temporal profile of short optical pulses," *Opt. Express* **16**, 3058–3068 (2008).
11. I. N. Ross, A. J. Langley, and P. Taday, "A Simple Achromatic Pulse Stretcher," CLF Annual Report 201–203 (1999–2000), RAL-TR-2000-034.
12. J. C. Stover, *Optical Scattering Measurement and Analysis*, 2nd. ed. (SPIE Publications. 1995), ISBN13:9780819477767.

Spatial overlap measurement of two F/2 parabolas on Astra-Gemini

Contact kristjan.poder@stfc.ac.uk

K. Poder, N. Booth, P. Brummitt, O. Chekhlov, K. Ertel, P.S. Foster, S. Hancock, S.J. Hawkes, P. Holligan, C.J. Hooker, D. Neely, D. Neville, B. Parry, D. Rathbone, D. Rose, D. Symes, Y. Tang, A. Zayyani, P.P. Rajeev

Central Laser Facility
STFC Rutherford Appleton Laboratory, Chilton, Didcot, OX11 0QX, UK

Introduction

As a preliminary test for an upcoming experiment a measurement of the spatial overlap of two focal spots produced by F/2 parabolas was done. In order to do this the parabolas were set up as depicted in Figure 1. The two spots were then optimized, first with a green 532nm expanded retro beam and then an 800 nm CW beam. During the optimization process, the camera in Figure 1 was in line with each beam.

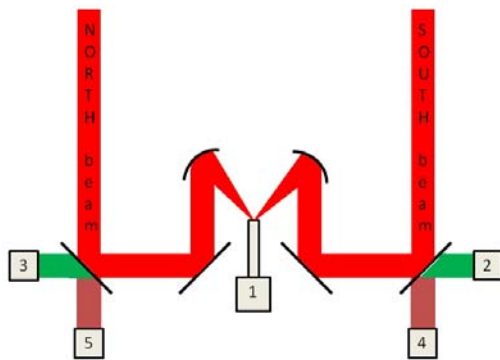


Figure 1. Setup used for the spatial overlap measurement; 1 is a CCD camera with a 50x microscope objective, 2 is south retro, 3 is north retro, 4 is south pointing monitor, 5 is north pointing monitor.

After both parabolas were optimized the camera was moved to the position depicted in Figure 1. The spots were moved to convenient locations on screen for ease of later analysis. A typical image acquired is shown in Figure 2. As the beams are being focused at an angle rather than normal incidence, calibration shots were taken to establish a scale in both horizontal and vertical direction. This was done separately for each beam.

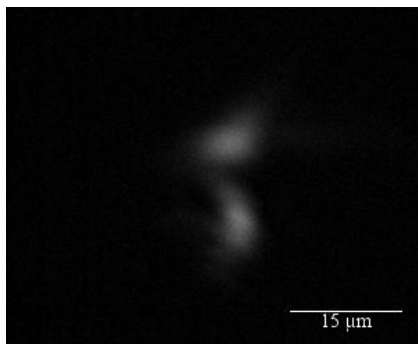


Figure 2. A typical captured image showing the north (upper) and south (lower) focal spots.

The measurements were done using the 10 Hz low power Astra beam. All cameras were turned onto external triggering. A clear relation between images from different cameras is then established, as all the shots are triggered off the same laser pulse. This enabled us to check for correlation between movements in pointing monitor spots and actual focal spots. In addition, CW retro beams for both north and south were optimized onto the CCD to analyze the origins of vibrations.

Another set of measurements was taken with the CW beam to check for any particular frequency patterns in the vibrations. Three different frequencies were used, namely 30, 60 and 175 Hz. All these measurements were done of the focal spots from the parabolas. The camera trigger setting used was internal, meaning images were captured at the closest possible to the specified frame rate.

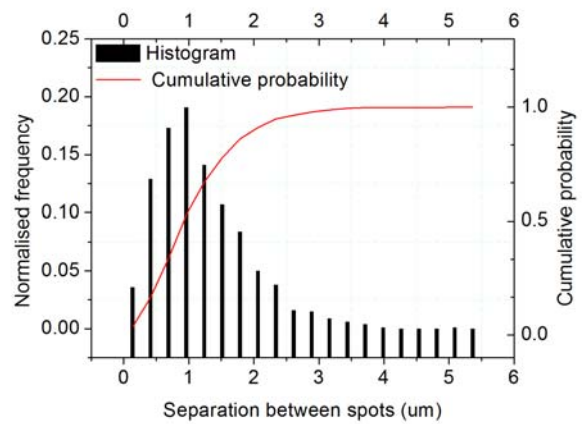


Figure 3. The separation between two focal spots: red line shows the cumulative probability to obtain a separation or less, black line is a histogram.

Results

To measure focal spot displacements, a set of around 500 images was acquired, and the centroid location was calculated for each spot. This was done on images of both focal spots and pointing monitor spots for both beams. A mean position was then found as an arithmetic average of both x and y coordinates. The displacements from the mean location are depicted in Figure 4. Numerically, the average deviation from mean position was calculated as $0.59 \pm 0.01 \mu\text{m}$ and $0.43 \pm 0.01 \mu\text{m}$ for north and south beam, respectively.

	Angle	Displacement
North	0.532	0.653
South	-0.320	0.568

Table 1. Correlation coefficients of north and south angular and linear displacements.

The displacements were then analyzed to determine the probability of achieving a certain focal spot overlap. This was done by calculating the separation between the centroids of focal spots for each image. A histogram is plotted in Figure 3, showing the normalized frequency of obtaining a certain separation between focal spots. A normalized cumulative histogram was also calculated. Also depicted in Figure 3, this gives a probability of obtaining a maximum separation between the focal spots.

In order to be able to predict the overlap of foci of a shot that had already taken place the pointing monitor spot locations were also analyzed. In this case, a drift vector \vec{r}_d was calculated as

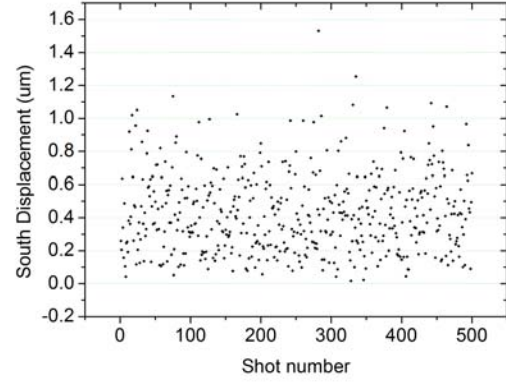
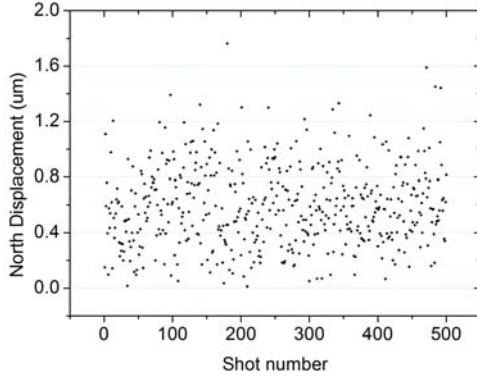


Figure 4. Displacement from mean position for both beams

$$\vec{r}_d = (x_i - x_{i-1}, y_i - y_{i-1})$$

where i is shot number. For each drift vector the length and angle are calculated as

$$|\vec{r}_d| = \sqrt{(x_i - x_{i-1})^2 + (y_i - y_{i-1})^2}$$

$$\theta = \arctan \frac{y_i - y_{i-1}}{x_i - x_{i-1}}$$

The angle will then be placed into the correct quadrant by adding either $\pi/2$, π or $3\pi/2$. To find correlations between displacement and angle changes, for each shot the value for focal spot is plotted against the value for pointing monitor. An example graph is shown in Figure 5. A linear fit line with a fixed intercept $b=0$ is also plotted. To get a more quantitative estimate of how the spots move, correlation coefficients were also calculated. These are listed in Table 1.

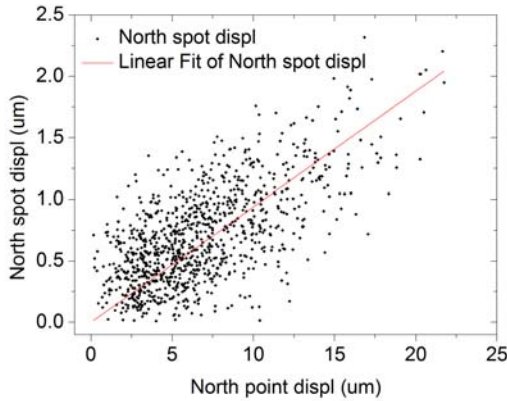


Figure 5. The displacement of focal spot plotted against displacement of pointing monitor.

The investigation into prominent frequencies occurring in vibrations was done by obtaining a typical set of about 2500 images. Again, the centroid coordinates were calculated. A Fast Fourier Transform (FFT) was then applied to both the x and y coordinate. According to the Nyquist-Shannon sampling theorem the maximum resolvable frequency is half of the sampling frequency^[1]. Hence the maximum detectable frequency was 87.5 Hz.

In order to check the origins of any vibrations, a separate set of data was taken with any possible sources turned off. These included vacuum chamber roughing pumps, turbo pumps, air-

compressor and diggers working on site near R7. The effects the changes had on frequency spectrum is shown in Figure 6.

Discussion

As described previously, the mean deviation from average spot position is of the order of half a micron. If the target is assumed not to move at all, then this would mean at least 16.7 % energy falls within a constant radius of the focal spot. When aiming for overlap of two spots, the distance between spot centres is relevant. For two 2.5 μm FWHM spots to achieve at least 75 % energy overlap, the maximum separation between spot centroids can be no more than 0.53 μm . The probability of achieving this is about 20 %.

The correlations between the focal spots and diagnostic monitors were quantified. The results show that the distance from the last shot location can be quite well evaluated with the pointing monitor. The angle, however, is much less correlated. Hence for each shot the distance between focal spots has to be assumed to be the worst, or that the beams moved at an angle π with respect to each other. This method sets the lowest value for energy overlap between spots.

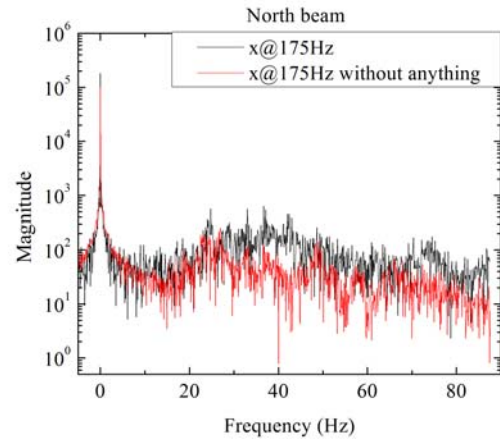


Figure 6. Frequency spectrum of vibrations of the focal spot with and without compressor, roughing pumps, turbos and diggers.

The FFTs performed on the data revealed relatively few aspects to vibration frequencies. There are discrepancies between frequency patterns from different frame rates. This is due to transfer rate fluctuations between camera and PC, some images were not saved hence leaving gaps in the dataset. When performing FFTs it is impossible to find out which images are actually missing and so the transform is performed on data with an essentially non-constant sampling rate.

In order to find certain sources of vibrations a set of measurements was taken with possible sources turned off. The likely things to cause vibrations were assumed to be the compressors, vacuum roughing pumps and turbo pumps. When all these were removed there was a slight improvement to

frequency spectrum of vibrations, however, the difference was not very big.

In order to eliminate the vibrations, or at least suppress them by a large amount, the implementation of a closed loop corrections system is being looked into. This system would use active feedback of both pointing and nearfield location of the beam and use actuated mirror mounts to correct for any sort of displacements.

References

1. C. Shannon, *Communication in the presence of noise*, Proceedings to the IRE, **37**, pp 10-21, 1949

Measuring and optimizing the pulse front tilt for Astra-Gemini Laser

Y. Tang, O. V. Chekhlov, C. Hooker, S. Hawkes, K. Poder, P. Foster and R. Pattathil

Central Laser Facility, STFC Rutherford Appleton Laboratory, Chilton, Oxon OX11 0QX, UK

Main contact email address:

Yunxin.Tang@stfc.ac.uk; Oleg.Chekhlov@stfc.ac.uk

Introduction & Background

During the development and commissioning of Astra-Gemini laser facility, almost all the ultra-high power laser aspects, such as pulse energy, beam quality, control of spectrum and residual high order spectral phase etc., have been addressed in order to achieve the design specifications, namely ultra-high power at PW level and ultra-high intensity up to 10^{22} W/cm². However, the residual angular dispersion due to misalignment of the stretcher and compressor in the chirped pulse amplification (CPA) laser systems could result in pulse front tilt (PFT). This will severely affect the laser performance [1,2,3] in terms of the pulse length and focal spot size in the far field. In this article we describe the basics of pulse front tilt measuring techniques and present some results of measurements of the Astra-Gemini laser beam. Application of the technique with a field inverted interferometer allowed further improvement of laser performance by optimizing the alignment of the stretcher and compressor to minimize the pulse front tilt.

Pulse front tilt description

In a CPA laser system, the alignment of stretcher and compressor is absolutely crucial. Usually the stretcher and compressor are aligned in-situ using a He-Ne laser or some other conventional optical method such as the far field image. These alignment methods have limited accuracy, and minor misalignments of the optical elements could cause residual dispersion that would give rise to substantial pulse front delay across the beam. The residual dispersion in CPA system usually originates when the diffraction gratings pairs in stretcher or compressors are not perfectly parallel. Misalignment of the gratings results in residual net angular dispersion in the ultra-short pulse laser beam, which causes the pulse front (maximum energy plane) to be tilted with respect to the wave front (constant phase plane) as illustrated below in Fig. 1.

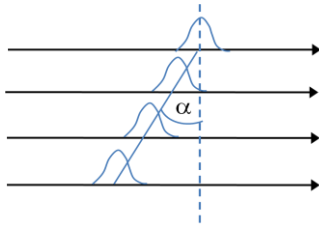


Figure 1 Pulse front tilt across a beam.

α is the angle between the pulse front and wave front, which is determined by [2]:

$$\tan \alpha = \lambda \frac{d\varepsilon}{d\lambda} \quad (1)$$

where λ is the mean wavelength and $d\varepsilon/d\lambda$ the angular dispersion [1,2]. As can be seen, the overall group delay over the beam is given by:

$$\Delta T = D \cdot \tan \alpha / c \quad (2)$$

where D is the beam size and c the speed of light. Larger beam sizes of high intensity CPA systems would be more susceptible to a small amount of uncompensated angular dispersion.

The pulse front tilt will obviously lead to the temporal broadening of the pulse in the focal plane due to the different arrival time at the focal point from the different parts of beam

along the pulse front tilt orientation, although the local pulse duration may not be affected by this pulse front tilt. At the focal point, the pulse intensity may be estimated by the electric field superposition of all parts of the beam along the pulse front tilt direction x as follows:

$$E(t) \propto \frac{4}{\pi D} \int_{-\frac{D}{2}}^{\frac{D}{2}} \sqrt{1 - \left(\frac{2x}{D}\right)^2} \exp\left(-2 \ln 2 \left(\frac{t - \frac{x \tan \alpha}{c}}{\tau_p}\right)^2\right) dx \quad (3)$$

where τ_p is the local pulse duration. Intensity $I(t) \propto E(t)^2$.

In addition, an angularly dispersed beam will also cause spatial spreading of the focal spot due to the spectral decomposition in the focal plane. For a top-hat beam, an enlargement of the focal spot in the angular dispersion direction may be approximated by:

$$\xi = 1 + \frac{\delta \lambda D \frac{d\varepsilon}{d\lambda}}{2.44 \lambda} \quad (4)$$

where ξ is the ratio of the enlarged focal spot to the diffraction limit, and $\delta \lambda$ the spectral bandwidth (FWHM).

The so-called ‘‘two-colour’’ method could be used to measure the angular dispersion in the ultra-short pulse laser beam. This is done by measuring the focal spot overlap of two isolated wavelength components located at both wings of the spectrum with a wavelength separation of $\Delta \lambda$. This method is simple and straightforward, but limited by the measurement resolution. Assuming $\frac{1}{2}$ focal spot size is the minimum distinguishable size on a CCD camera when two focal spots were overlapped, the minimum angular dispersion that could be detected by this method is given by:

$$\frac{d\varepsilon}{d\lambda} \geq \frac{1}{2} \eta \theta_{diff} / \Delta \lambda \quad (5)$$

where η is defined as the quality of the diagnostic optics and θ_{diff} the diffraction limit angle. For example, at the Astra-Gemini diagnostic table, the full 150mm beam size is used to measure the far field of the compressed pulse with an aberration

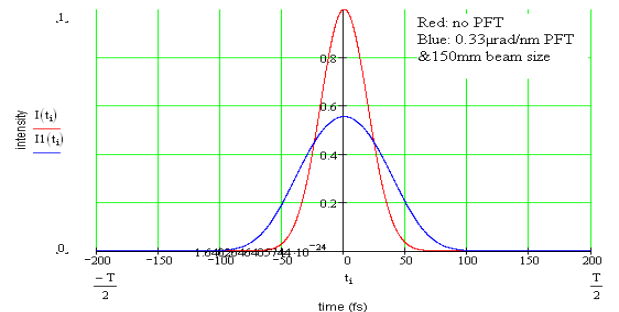


Figure 2. Temporal broadening at the focal point due to PFT

of ~ 2 times of diffraction limit. For a typical wavelength separation of ~ 40 nm used in the two-colour method, the dispersion is $\sim 0.33 \mu\text{rad/nm}$ according to (5). This minimum angular dispersion sounds rather small but it would produce a significant pulse front tilt angle of ~ 0.27 mrad and overall group delay of ~ 135 fs over the 150mm Gemini laser beam. With such a small angular dispersion the temporal broadening of a ~ 45 fs laser pulse at the focal point might be approximated according to (3) and illustrated in Fig. 2.

This small residual angular dispersion also results in a one-dimension spatial broadening in the far field with an estimated factor of ~ 2 based on (4), and hence reduces the intensity in the focal plane even further. More rigorous and detailed analysis of the effect of angularly chirped pulse on the temporal intensity in the focal plane can be found in [3].

Results and discussion

In order to improve the angular dispersion measurement accuracy and overcome the limitations of other alignment techniques, a field-inverted interferometric autocorrelator (FIAC) was implemented to measure the pulse front tilt as shown in Fig. 3. It can be shown that the delay between the two pulses is given by: $\Delta\tau = \Delta d\sqrt{2}/c$, where c is the speed of light.

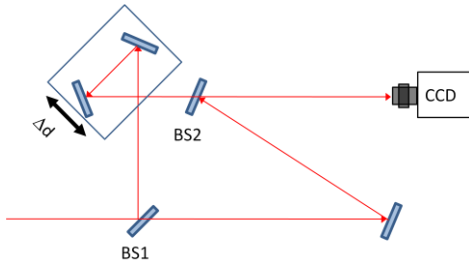


Figure 3 Schematic of FIAC

As one of the pulse replicas in the FIAC is spatially inverted, the delay between the two pulse replicas is position-dependent along the pulse front tilt direction across the beam if the pulse front is tilted. This position-dependent delay can be detected by the spatial interference pattern, as interference will only occur at positions in the beam where the two replicas overlap. Analysis of the visibility of interference fringes as a function of delay gives a quantitative measurement of the pulse front tilt.

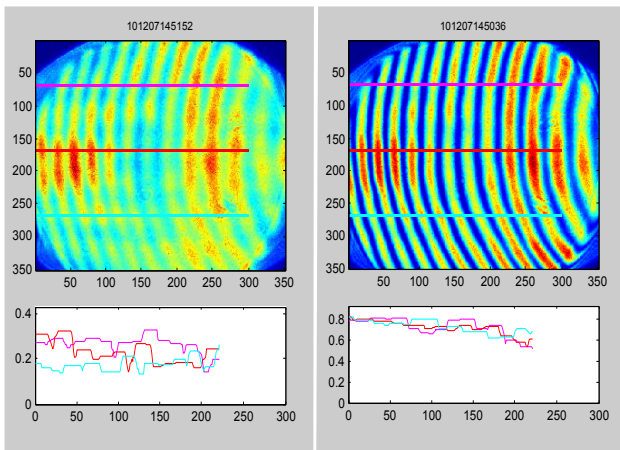


Figure 5 Examples of interferogram at different time delays (top) and visibility profile lines (bottom) spatially sampled from corresponding lines of interferograms.

Experimentally the beam from Gemini was measured at different places using the FIAC. Firstly it was measured after the stretcher, with a 5x beam expanding telescope, and then before the 3x expander, where the beam diameter is 50mm, and finally after the compressor. Taking measurements at different places allows us to monitor and minimize the amount of residual dispersion along the amplification chain. Even though the beam size of 150mm after the compressor is larger than the 4th optics used in the FIAC, our analysing technique allowed us to retrieve the pulse front tilt quite accurately from images of interferograms of slightly truncated beams. It is worth noting that the pulse front tilt was measured both in vertical and horizontal directions, corresponding to the main dispersion and groove orientation directions of the compressor gratings, respectively.

The change of visibility of interference fringes across the laser beam can be seen from the images and corresponding plots in Fig.4. The images in Fig. 4 are rotated by 90 degrees for presentation purposes. The right hand image corresponds to a relative delay which is close to zero. The visibility data taken from this image are quite similar to each other, as seen from the plots at the lower right in Fig.4. The left-hand image corresponds to a delay of tens of femtoseconds away from zero. The change of visibility is noticeable from lower left plots in Fig.4.

To achieve a quantitative measurement of the pulse front tilt, the visibility dependences on time delay were retrieved from a series of images, and these are presented in Fig.5. The visibility data were sampled from the images along the lines with corresponding colours. The change of temporal position of the maximum of visibility is directly connected to the spatial pulse front tilt while the zero point of interference moves across the field.

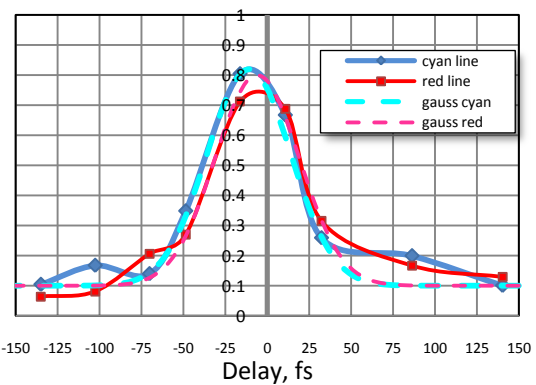


Figure 4 Dependences of interference fringe visibility on time delay of field inverted interferometer. Dashed lines are Gaussian fits to the experimental data.

By finding the delay between different parts of the beam it was possible to evaluate the residual angular dispersion. The retrieved delay between two dependences presented in fig.5 was 9 fs between the red and cyan lines in fig.4. This corresponded to a pulse front tilt of 37.8 fs for the whole 150 mm beam. The angular dispersion derived from this tilt was 9.45×10^{-8} rad/nm. This amount of angular dispersion would be responsible for 8.5 μ m spread of the focal spot of a beam with a 30nm wide spectrum focused by a 3000mm focal length lens. It would be hardly visible from the shape of the focal spot given that the Airy radius of a diffraction limited spot is $\sim 19.4 \mu$ m. The amount of the pulse front tilt presented in Fig.4 and 5 was easily detectable using the FIAC and was minimized by corresponding adjustments of the compressor gratings.

Conclusions

The pulse front tilt of both stretched and compressed pulse beams of the Gemini laser system was measured using a field inverted autocorrelator. A simple retrieval technique for data analysis of the interferograms substantially improved the accuracy of the pulse front tilt and residual dispersion measurements. Optimization of stretcher and compressor alignment by minimizing the pulse front tilt resulted in further enhancement of laser performance.

References

1. Z. Bor B.Racz, G. Szabo, M. Hilbert, H.A. Hazim . Opt.Engineering ,**32**.,2501 (1993).
2. J. Hebling, Opt. and Quantum Electron. **28**, 1759 (1996).
3. G. Pretzler, A. Kasper and K.J. Witte, Appl. Phys. B **70**, 1 (2000).